MATERIALS SCIENCE

Imaging and simulation of surface plasmon polaritons on layered 2D MXenes

Janek Rieger[1], Atreyie Ghosh[1], Joseph L. Spellberg[1,2], Calvin Raab[1,2], Aishani Mohan[2], Prakriti P. Joshi[1]†, Sarah B. King[1,2]*

Two-dimensional (2D) transition metal carbides and nitrides, commonly known as MXenes, are a class of 2D materials with high free carrier densities, making them highly attractive candidates for plasmonic 2D materials. In this study, we use multiphoton photoemission electron microscopy (nP-PEEM) to directly image the plasmonic near fields of multilayers of the prototypical MXene, $Ti_3C_2T_x$, with mixed surface terminations (T_x = F, O, and OH). Photon-energy dependent nP-PEEM reveals a dispersive surface plasmon polariton between 1.4 and 1.9 electron volts on MXene flakes thicker than 30 nanometers and waveguide modes above 1.9 electron volts. Combining experiments with finite-difference time-domain simulations, we reveal the emergence of a visible surface plasmon polariton in MXenes, opening avenues for exploration of polaritonic phenomena in MXenes in the visible portion of the electromagnetic spectrum.

INTRODUCTION

MXenes are a class of two-dimensional (2D) transition metal carbides and nitrides with the formula $M_{n+1}X_nT_x$, where M represents a transition metal, X is either carbon or nitrogen, and T_x denotes surface terminations. Modification of the transition metal and surface terminations enables wide tunability of MXene optoelectronic properties (1–3), allowing customization for applications that include energy storage, sensing, and catalysis (4–6). Notably, many MXenes are 2D metals with high charge carrier densities. The most commonly investigated MXene is $Ti_3C_2T_x$ with mixed surface terminations (T_x = F, O, and OH), which exhibits metallic conductivity and free charge carrier densities of up to 3×10^{22} cm^{-3} (7). Such high free charge carrier densities could enable plasmonic excitations in the visible and ultraviolet (UV) portion of the electromagnetic spectrum in these 2D metals.

Localized surface plasmons and surface plasmon polaritons (SPPs) of 3D metals have been used for applications such as photocatalysis, spectroscopy, and sensing, as plasmonic resonances enable subwavelength confinement of electromagnetic fields (5, 8–12). 2D plasmonic materials, such as graphene and metallic transition metal dichalcogenides, can provide an even stronger field enhancement than 3D plasmonic metals and display unique properties due to their decreased dielectric screening and structural anisotropy (13). Graphene and other 2D materials are also attractive because their plasmon resonances can be tuned by gating or doping. However, their plasmonic resonances are typically limited to the mid-infrared region of the electromagnetic spectrum, and they have limited tunability for surface chemistry and plasmon-enhanced catalysis (13–17). Not only can MXenes support plasmons, but also they offer tunability of plasmonic excitations (18, 19), surface reactivity (1, 3), and processing (20). Tuning the surface terminations of MXenes is particularly promising because it allows altering their surface reactivity. Many MXenes such as $Ti_3C_2T_x$ are hydrophilic due to their surface terminations, which makes them attractive for large-scale thin film preparation, coating, printing, as well as plasmonic-enhanced sensing and catalysis in solvents (20, 21). Therefore, MXenes could serve as platforms for plasmon-enhanced catalysis, provided that they display suitable dielectric properties.

Plasmons require the real component of the frequency-dependent complex dielectric function, $\varepsilon(\omega) = \varepsilon'(\omega) + i\varepsilon''(\omega)$, to be less than zero $[\varepsilon'(\omega) < 0]$. Recent ellipsometry measurements on $Ti_3C_2T_x$ thin films suggest that $\varepsilon'(\omega)$ is mostly negative below 1.9 eV (22, 23), and single $Ti_3C_2T_x$ flakes are expected to exhibit plasmonic responses up to 1.9 eV. The ability of MXenes to transform applications such as plasmon-enhanced catalysis depends on the exact nature of these plasmonic responses; only plasmon resonances can confine light effectively. Previous electron energy-loss spectroscopy (EELS) measurements on $Ti_3C_2T_x$ have provided experimental evidence for dispersive surface plasmons in the infrared region with a corresponding surface plasmon resonance at 600 to 900 meV (24, 25). A peak observed between 1.7 and 2.0 eV was assigned to a transversal plasmon resonance in some studies, but it is unclear how such a transversal mode can exist in MXenes because of their 2D geometry and band structure (23, 24, 26). Other studies have suggested that this resonance is not associated with plasmonic excitation but rather is an interband transition (7, 25, 27). Whether and how $Ti_3C_2T_x$ MXenes can support surface plasmon resonances in the visible portion of the electromagnetic spectrum are critical questions for the development of MXene plasmonics.

Here, we use multiphoton photoemission electron microscopy (PEEM) to directly image surface plasmons and waveguide modes of single $Ti_3C_2T_x$ flakes. PEEM is a wide-field electron microscopy technique with a spatial resolution of less than 10 nm, which is based on the photoelectric effect (28). Multiphoton PEEM (nP-PEEM; where n is the number of photons) gives direct access to the local electronic surface structure, local transition dipoles, as well as the electric near fields from surface plasmons, waveguide modes, and photonic modes (29–36). It has been extensively used to study SPPs on noble metal surfaces (37–39). We have previously used nP-PEEM to study the electronic properties of 2D materials (34, 35). Here, we image dispersive SPPs and waveguide modes of a layered 2D material, $Ti_3C_2T_x$. We image the energy-dependent near-field

[1]James Franck Institute, University of Chicago, Chicago, IL 60637, USA. [2]Department of Chemistry, University of Chicago, Chicago, IL 60637, USA.
*Corresponding author. Email: sbking@uchicago.edu
†Present address: Department of Physical Chemistry, Fritz Haber Institute of the Max Planck Society, Faradayweg 4-6, 14195 Berlin, Germany.

response of isolated multilayer $Ti_3C_2T_x$ flakes over the entire visible frequency range, between 1.45 and 3.42 eV. We find that $Ti_3C_2T_x$ flakes exhibit a dispersing surface plasmon up to 1.9 eV, but do not observe a corresponding surface plasmon resonance, when they are thicker than 30 nm. Above 1.9 eV, $Ti_3C_2T_x$ exhibits waveguide-like behavior.

RESULTS

$Ti_3C_2T_x$ flakes shown schematically in Fig. 1A were synthesized and deposited on silicon wafers with native oxide for nP-PEEM imaging as described in Materials and Methods section. Figure 1 (B to E) illustrates the excitation geometry for nP-PEEM measurements. Two different light sources are used for PEEM imaging, grazing incidence excitation in a single-photon photoemission process (1P-PEEM) with a Hg arc lamp or normal incidence excitation with an ultrafast laser in an nP-PEEM. The imaging contrast in nP-PEEM arises from the spatially varying photoemission yield across the sample surface, which is imaged with electron lenses in the PEEM column. 1P-PEEM uses UV photons to directly excite photoelectrons from the occupied valence states below the Fermi level, E_F, into final states above the vacuum level, E_{vac} (see Fig. 1, B and C). With 1P-PEEM, an image of the surface structure is generated that depends on the local work function, the local joint density of states, and the sample's topography. Figure 1F shows a 1P-PEEM image of $Ti_3C_2T_x$ flakes on a Si/SiO₂ substrate. Two MXene flakes (flake 1 and flake 2) can be identified. The metallic MXene flakes appear brighter than the Si/SiO₂ substrate because the MXenes have a lower work function and an increased density of states around the Fermi level (29, 40, 41). Additional intensity variations across the MXene flakes, for example, at the left edge of flake 1, are caused by inhomogeneities of the flake topography, such as surface roughness, and by potentially associated variations of the electronic structure (see Fig. 2E and fig. S1).

Local electric fields from surface plasmons, waveguides, and diffraction on the sample surface can be imaged with nP-PEEM if more than one photon is used for excitation (Fig. 1, B, D, and E) (29–33, 39, 42). The nonlinear photoexcitation requires high fluences that are provided by pulsed laser sources. When the laser's angle of incidence on the sample is near normal, the intensity variations in the nP-PEEM images correspond directly to the spatial oscillations of local fields at the surface (33, 43). Representative images of 3P-PEEM
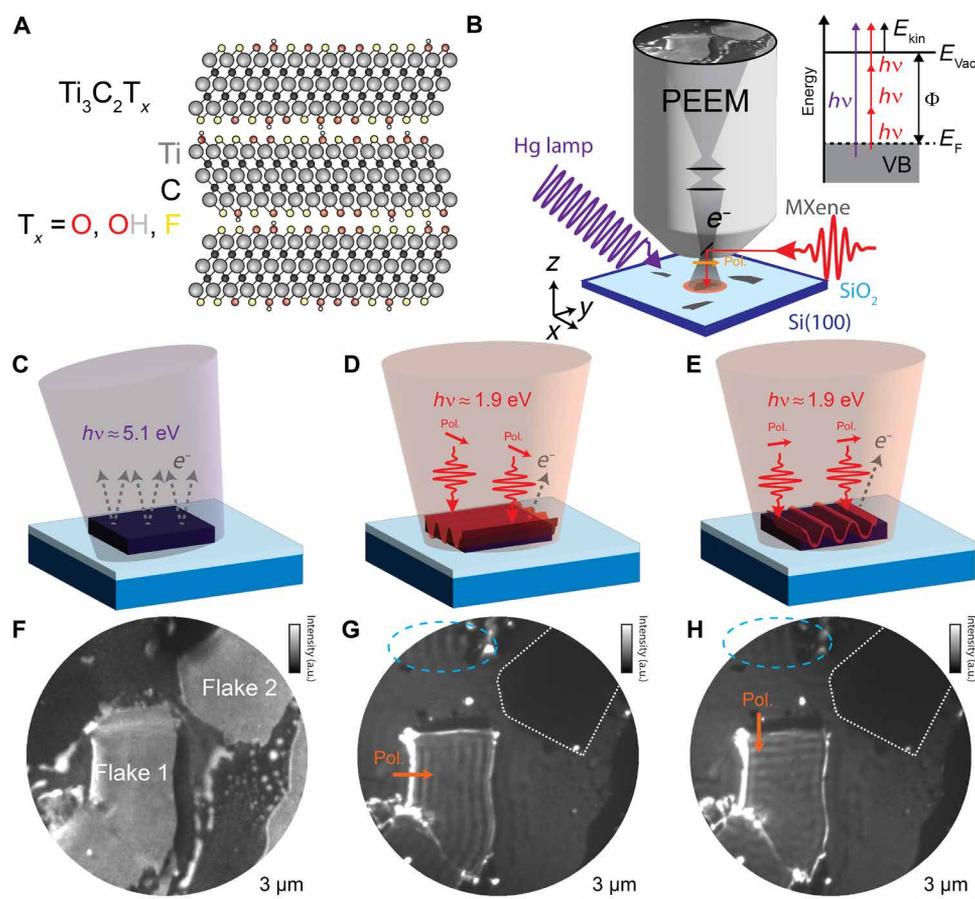
Fig. 1. Schematic of sample, measurement configuration, and overview of *n*P-PEEM results on MXene flakes. (**A**) Stacks of multilayer $Ti_3C_2T_x$. (**B**) Geometry of the PEEM instrument including the grazing incidence illumination with a Hg arc lamp and the near-normal illumination with a laser. The inset illustrates the photoexcitation and involved energy levels in 1P-PEEM and 3P-PEEM. (**C** to **E**) Illumination geometries for the *n*P-PEEM images presented in (F) to (H). (C) Illumination with an Hg lamp in grazing incidence. (D and E) Illumination with a pulsed laser source in near-normal incidence. (**F**) 1P-PEEM image of two selected MXene flakes on Si/SiO₂. (**G** and **H**) The 3P-PEEM images of the same flakes that were recorded with two different laser polarizations (see arrows). The blue dashed ellipses in (G) and (H) emphasize fringes on the substrate. a.u., arbitrary units.
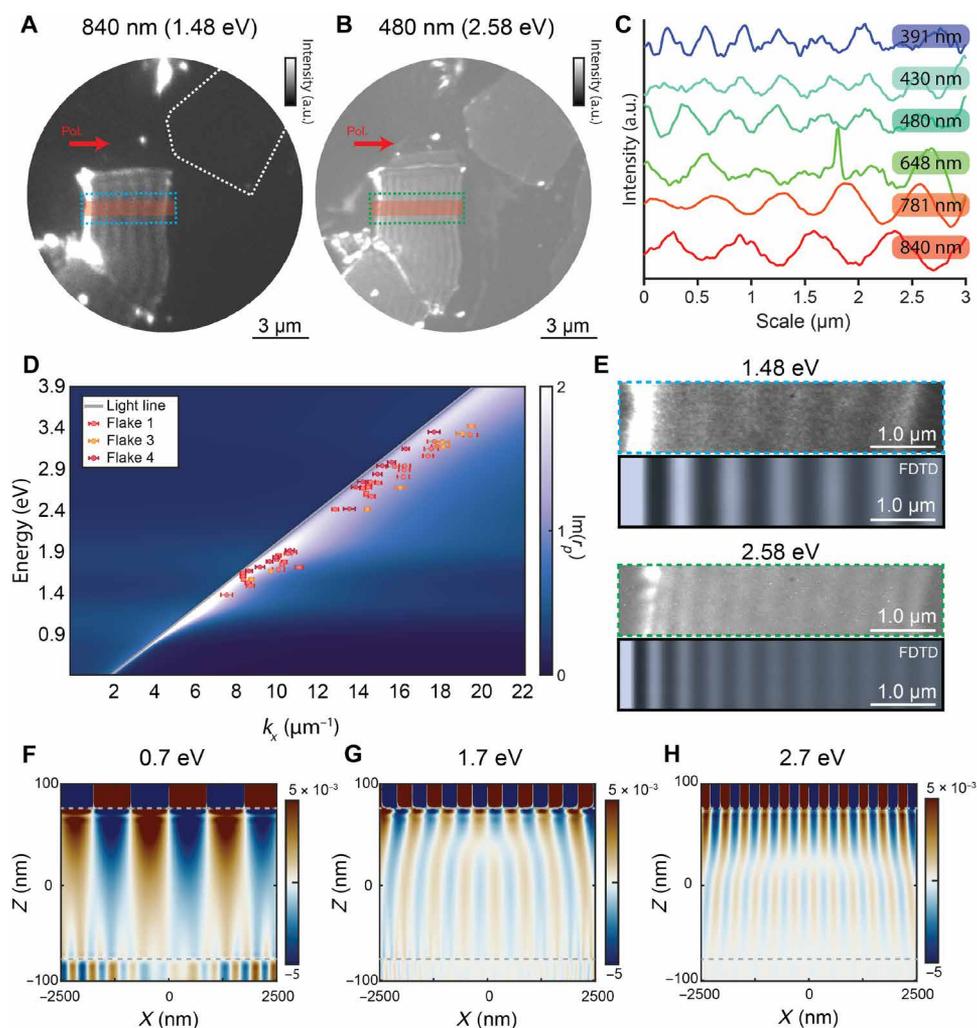
Fig. 2. Wavelength-dependent *n*P-PEEM and *n*P-PEEM simulations on Ti₃C₂Tₓ. (**A**) Representative 4P-PEEM image excited with 840 nm (1.48 eV). (**B**) Representative 2P-PEEM image excited with 480 nm (2.58 eV). (**C**) Linecuts from wavelength-dependent *n*P-PEEM measurements. Energy-dependent wave vectors extracted from the line cuts for three different MXene flakes are plotted on top of a heat map in (**D**) of the imaginary part of the reflection coefficient of the sample. (**E**) Comparison of regions of interest from experimental PEEM images in (A) and (B) with FDTD simulated *n*P-PEEM images of 160-nm-thick Ti₃C₂Tₓ on silicon with native oxide at 1.48 and 2.6 eV. (**F** to **H**) Side view of the simulated distribution of the E_z fields across the 160-nm-thick Ti₃C₂Tₓ flake for three selected energies. The surface and interface with the substrate are indicated by gray dashed lines.

from flake 1 and flake 2 for excitation with two different laser polarizations at near-normal incidence are shown in Fig. 1 (G and H). The laser polarizations were chosen such that they are perpendicular to the edges of flake 1 (Fig. 1, D and E).

The 3P-PEEM images show three differences from the 1P-PEEM image in Fig. 1F. (i) Flake 1 in the center of the 3P-PEEM image remains bright, while the photoemission from flake 2 at the top right of the image is strongly suppressed. (ii) Flake 1 exhibits fringes on its surface, observed as periodic intensity modulations in the *n*P-PEEM image, while flake 2 does not. The direction of the fringe wave vector depends on the laser polarization. Fringes are launched at a flake edge when the laser polarization is aligned perpendicular to the edge. Fringes are also launched at the boundary between flake 1 and its neighboring flake. (iii) Additional fringes with larger spacing appear on the substrate beside the MXene flakes (marked by a blue dashed ellipse in Fig. 1, G and H). These fringes can only be imaged

when the photoemission intensity from the substrate is high compared to the photoemission intensity from the flakes (compare Figs. 1G and 2A). They do not show a laser polarization dependence like the fringes on top of the MXene flakes. These interference bands stem from a diffraction pattern on the substrate. The edges of the MXene flake diffract the incoming light, and the substrate acts as a screen on which the diffraction pattern can be observed (*29*, *30*, *42*).

Energy-dependent *n*P-PEEM measurements were performed to study the dispersion relation of the fringes on top of flake 1. Figure 2 (A and B) shows *n*P-PEEM images that were taken with an excitation energy of 1.48 and 2.60 eV, respectively. The spacing of the fringes decreases with increasing photon energy. Selected linecuts from the wavelength-dependent *n*P-PEEM measurements are shown in Fig. 2C. These linecuts were fit with the function $f(x) = A_0 \cdot e^{-\ell x} \cdot \sin(k_x x - \phi) + bx + c$ to determine the energy-dependent wave vectors k_x; all fits are available in the Supplementary

Materials. A_0 is the initial amplitude, ℓ is the decay constant, ϕ is the phase of the fringes with respect to the coordinate x, and k_x is the wave vector. The last two terms approximate the photoemission background from the flake. Figure 2D shows the resulting dispersion relation by plotting the excitation energy versus the fitted wave vector. Dispersion relations of three MXene flakes are shown with error bars on top of a color map (see figs. S2 and S3 for examples of nP-PEEM images from flake 3 and flake 4). The color map corresponds to the magnitude of the imaginary part of the reflection coefficient of the whole sample stack assuming real wave vectors, with its maxima resembling the sample's potential polaritonic surface and waveguide modes (44). The experimentally determined dispersion from our nP-PEEM experiments largely matches the theoretical expectations from the reflection coefficient (see Fig. 2D). Deviations may arise from the slightly varying dielectric function of individual MXene flakes, the fact that the dielectric function was determined with a disordered thin film, and potential adsorbates on the MXene surface that may shift the dispersion of surface modes to higher wave vectors (45–48).

A more detailed understanding of the electric fields at the surface can be derived from finite-difference time-domain (FDTD) simulations. These simulations determine the time- and spatially resolved electric field components E_x, E_y, and E_z within the investigated sample, with dominant contributions from E_x and E_z components for incident light polarization along the x direction. nP-PEEM images can be simulated by the temporal integration of the calculated fields (49, 50). The simulated images in Fig. 2E, calculated with the reported dielectric function of $Ti_3C_2T_x$ (23), reproduce the measured nP-PEEM images well. Figure 2 (F to H) shows the side view (xz plane) of the E_z distribution at three different energies. Positive and negative field components are shown as red and blue, respectively (51, 52). The sign of E_z oscillates parallel to the surface at all energies, as expected from the observed fringes in the simulated nP-PEEM images. The periodicity of the oscillations is always larger at the surface than at the substrate interface (see Fig. 2F). Two major differences can be identified in the energy-dependent simulations. First, the field modulation at the substrate interface is much more prominent at 0.7 eV compared to the other two energies. Second, E_z changes its sign perpendicular to the surface at 0.7 eV and 1.7 eV, but not at 2.7 eV.

All observed fringes on $Ti_3C_2T_x$ flakes correspond to transverse magnetic (TM) modes, as they are only excited when the laser polarization is parallel to the wave vector of the fringes but perpendicular to the flake edge (Fig. 2 and figs. S2 and S3) (32, 33). No transverse electric modes are observed, which would be excited with a laser polarization parallel to the flake edge (32).

We will first discuss the origin of the TM modes for energies <1.9 eV. At these energies, the field component E_z in FDTD simulations changes its sign perpendicular to the surface, indicating monopolar charges at the surface (see Fig. 2, F and G). Such surface charges are a unique fingerprint of SPPs (39). SPPs are caused by the displacement of charges at the interface between a solid-state plasma and a dielectric (33, 53). They can only exist at interfaces between two materials where $\varepsilon'(\omega)$ of each material has opposite signs. The momentum of SPPs is always larger than that of vacuum light, i.e., SPPs disperse to the right of the light line (see Fig. 2D). In PEEM, SPPs are excited by light at an interface of a metal with vacuum, and the momentum required for SPP excitation is supplied by discontinuities such as edges or slits. SPPs are TM surface waves and

are only excited by laser field components that are parallel to k_x (33). That is why the observed fringes on the $Ti_3C_2T_x$ flakes are launched from the edges when the laser polarization is perpendicular to the edge orientation.

Further evidence for this assignment comes from the differing behaviors of flake 1 and flake 2 in nP-PEEM at energies below 1.9 eV. Flake 1 shows both fringes and substantially higher photoemission intensity compared to flake 2 (see Fig. 2, A and B). This discrepancy cannot be attributed to variations in surface electronic structure, as both flakes have similar work functions and surface electronic structures (see fig. S6). The only noticeable difference between the two MXene flakes is their thickness: Flake 1 is 160 nm thick, and flake 2 is 25 nm thick (see fig. S1).

To understand the differences between the two flakes and the impact of flake thickness, we must consider the thickness-dependent behavior of SPPs in metal thin films. Both interfaces of a metal thin film can support SPPs, and these SPPs can interact with each other if the film is thinner than 250 nm (32, 53, 54). Figure 3 illustrates how SPPs from the upper and lower interfaces interact in very thin films. This interaction leads to the formation of two bound supermodes with (a)symmetric field distributions (Fig. 3, A and B), which are highly sensitive to the film's thickness and the dielectric environment at each interface (53–55). Their dispersion is presented in Fig. 3D for a 30-nm-thick metal film surrounded by vacuum. Note the dispersion in Fig. 3D is only a model to illustrate the impact of thin-film modes and is not intended to reflect the plasma frequencies of the MXene studied. The asymmetric SPP mode (red dots) disperses up to the surface plasmon resonance and then bends back toward the light line. The symmetric mode (green dots) disperses close to the light line and shows slight deviation from the light line close to the bulk plasmon energy. When the thin metal film is embedded between two dielectric media with different dielectric functions (asymmetric cladding), each super-mode becomes localized closer to one of the two interfaces (see Fig. 3C and fig. S4). The symmetric mode resides closer to the interface with the lower permittivity, while the asymmetric mode is positioned nearer to the interface with the higher permittivity. Please note that we use the standard optics convention where symmetric and asymmetric modes are determined by the spatial distribution of the main transverse electric field, E_z (55).

This scenario can be used to describe the thin MXene film on Si/SiO$_2$ surrounded by vacuum used in our experiments. The FDTD simulations of E_z at 0.7 eV shown in Fig. 2F exhibit both modes. The symmetric mode at the surface of $Ti_3C_2T_x$ has a larger wavelength than the asymmetric mode at the interface to the substrate. nP-PEEM is highly surface sensitive, probing mostly the bound super-mode located on the MXene film's vacuum side. The other mode can only be observed in specific geometries and on thinner films in nP-PEEM (56–58).

The two super-modes and their interactions are highly sensitive to the flake's thickness. Figure 4 (A and B) compares simulated nP-PEEM images for $Ti_3C_2T_x$ flakes of different thicknesses, specifically 160 and 25 nm, on Si/SiO$_2$. In line with experimental results, the 160-nm-thick MXene flake exhibits higher photoemission intensity at energies below 1.9 eV compared to the 25-nm flake, assuming the same dielectric function for both. This difference arises because the super-mode on the vacuum side of the MXene flake is only bound to the interface when the film's thickness is above a critical value (59, 60). The critical thickness is determined by calculating the
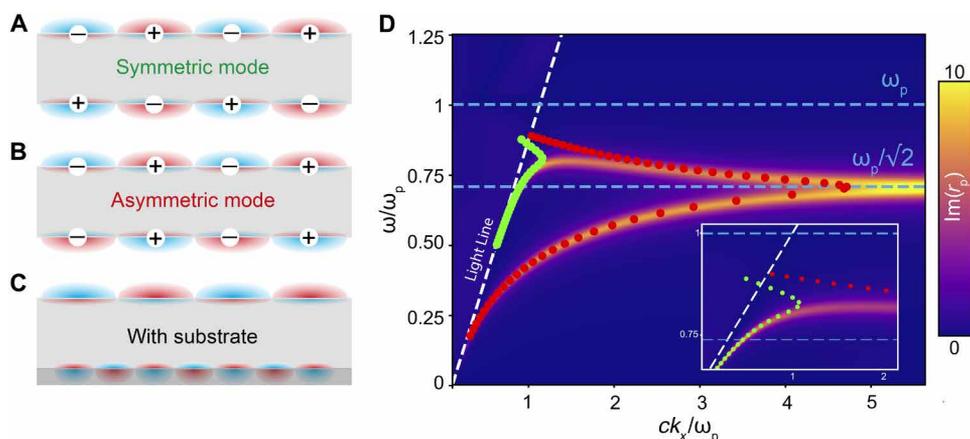
Fig. 3. Illustration of the two metallic thin film SPP modes. (**A** and **B**) Schematic field distributions of the symmetric and asymmetric SPPs of an ideal metallic thin film in vacuum at constant wave vector k_x. (**C**) Schematic field distributions of symmetric (surface) and asymmetric (interface to substrate) SPP at a constant energy when the metallic thin film is located on a substrate in vacuum. (**D**) Dispersion of the two SPP modes assuming an illustrative model Drude-metal thin film with losses ($\omega_p = 4$ eV, $\gamma = 0.2$ eV, $d = 30$ nm, $\epsilon_\infty = 1$) in vacuum. The bulk plasmon energy (ω_p) and surface plasmon resonance ($\omega_p/\sqrt{2}$) for a semi-infinite film are indicated with light blue dashed lines. The light line is indicated by a white dashed line. Numerical solutions for the two SPP modes are shown as red (asymmetric mode) and green (symmetric mode) dots, respectively. The color plot shows the imaginary part of the reflection coefficient $\mathrm{Im}(r_p)$ assuming real wave vectors k_x.
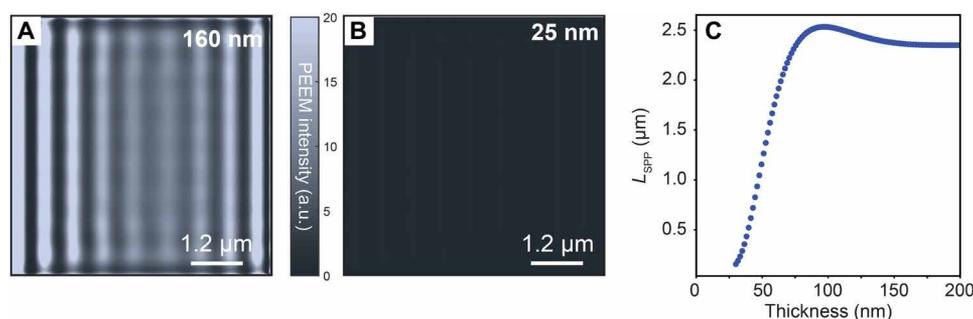
Fig. 4. Simulations of Ti$_3$C$_2$T$_x$ with varying thickness. FDTD simulated nP-PEEM images of Ti$_3$C$_2$T$_x$ on silicon with native oxide at 1.7 eV of (**A**) 160-nm and (**B**) 25-nm-thick flakes. (**C**) Thickness-dependent propagation lengths of symmetric thin film SPP on Ti$_3$C$_2$T$_x$ between vacuum and Si/SiO$_2$.

propagation constants of the super-mode, based on the dielectric function of Ti$_3$C$_2$T$_x$ (*32*). As shown in Fig. 4C, the thickness-dependent propagation constants $L_{\mathrm{SPP}} = (\mathrm{Im}\,k_x)^{-1}$ of the symmetric SPP at 1.7 eV in a four-layer structure, with Ti$_3$C$_2$T$_x$ embedded between vacuum and Si/SiO$_2$, reveal a cutoff thickness of ~30 nm. Consequently, the symmetric SPP is supported only in MXene flakes thicker than 30 nm.

This explains the thickness-dependent photoemission intensity and why fringes are observed only on flake 1. In the thinner flake 2, the absence of an SPP at the MXene/vacuum interface leads to a lack of fringes and the associated enhanced local electric field that typically boosts multiphoton photoemission (*33*). As a result, flake 2 appears dark in the nP-PEEM measurements at energies below 1.9 eV. This effect is particularly pronounced at low-photon energies, especially below 1.6 eV, where four photons are required for photo-excitation (see Fig. 2A and fig. S6).

Last, we observe an interference pattern in nP-PEEM images when conducted at grazing incidence (see fig. S7) with a different periodicity than at normal incidence. This is characteristic of SPPs in nP-PEEM experiments due to light-plasmon interference (*32, 43, 61*).

Now, we turn to the origin of the fringes for energies 1.9 eV. At these energies, the fringes in the nP-PEEM images cannot be assigned to SPPs, because $\varepsilon'(\omega)$ is positive at energies >1.9 eV (see fig. S4). Consistently, Ti$_3$C$_2$T$_x$ is mostly transparent in the visible region, as can be seen in the optical images of the investigated flakes (see figs. S1 to S3). If surface plasmons were present at >1.9 eV, then Ti$_3$C$_2$T$_x$ would reflect more portions of visible light and have reduced transparency in the visible region. Therefore, the fringes at >1.9 eV must stem from waveguide modes of the MXene thin film. This hypothesis is further supported by the behavior of E_z calculated with FDTD simulations (see Fig. 2H). The sign of E_z does not change at the surface at >1.9 eV because there are no monopolar charges at the surface. Instead, a nodal pattern can be observed across the thin film, which is characteristic of waveguide modes (*32, 54*).

DISCUSSION

To our knowledge, this is the first observation of an SPP on MXenes up to 1.9 eV. This extends the plasmonic properties of MXenes into portions of the visible region of the electromagnetic spectrum. Previous EELS experiments found dispersive surface plasmons with a

plasmon resonance in the infrared (<1 eV) on $Ti_3C_2T_x$ (24, 25, 62). While these two observations seem contradictory at first glance, they are fully consistent when considering the thin-film model needed to describe the plasmonic properties of MXenes. The reported EELS experiments were mostly carried out on MXene films (<20 nm) that were thinner than the critical thickness to support the symmetric mode and should only exhibit the asymmetric energetic plasmon mode (24, 25, 62). In contrast, the nP-PEEM experiments discussed here were conducted on thicker MXene flakes deposited on a silicon substrate with native oxide. The asymmetric dielectric environment causes the symmetric mode to shift toward the vacuum side.

The second reason why the symmetric SPP mode is not observed with EELS is because of the absence of a corresponding plasmon resonance. The symmetric SPP disperses close to the light line for energies below 1.9 eV (see Figs. 2 and 3D). Without this resonance, only a very weak signal of this mode could be detected in EELS, even in MXene films thicker than the critical thickness. Additionally, the symmetry of its electric fields results in a low EELS probability for the higher energy mode in very thin films (63).

Early EELS experiments on $Ti_3C_2T_x$ assigned a peak in the visible between 1.7 and 2.0 eV on thin $Ti_3C_2T_x$ flakes to a transversal plasmon resonance (24). There is no experimental evidence of such a mode in our nP-PEEM images on $Ti_3C_2T_x$ flakes with lateral sizes of several microns. No clear plasmon resonance can be observed in the experimentally determined dispersion around that energy. Consistently, the hypothesized transversal plasmon resonance is not present in FDTD simulations. From a theoretical point of view, no transversal mode would be expected on an infinitely wide metallic thin film. Metallic thin films are only expected to exhibit two SPP supermodes as long as they are thicker than a critical thickness (53). Additional modes might be observed in thin metal films with finite lateral dimensions, but they should be observable as standing waves in microscopic measurements and are not associated with transversal modes (60, 63, 64). The peak previously observed with EELS possibly stems from an interband transition at 1.7 to 2.0 eV that is reported in ellipsometry experiments (22, 23, 65).

While our experimental results are described fairly well by an isotropic dielectric function of $Ti_3C_2T_x$ (see Fig. 2D), we would like to point out that $Ti_3C_2T_x$ is a layered material. Therefore, an anisotropic dielectric function would describe $Ti_3C_2T_x$ better (27, 66). It is likely that the anisotropy in $Ti_3C_2T_x$ is weaker than in van der Waals materials due to the hydrogen bonds between single $Ti_3C_2T_x$ layers (67). nP-PEEM images were simulated using both an isotropic and a strongly anisotropic dielectric function (see fig. S8). The fringes on $Ti_3C_2T_x$ become slightly more pronounced when simulated with an anisotropic dielectric function at <1.9 eV. However, the wave vectors of the measured modes are not markedly influenced by the anisotropy. Hence, the anisotropy is not critical to the presented nP-PEEM measurements and does not change our interpretations and conclusions.

In summary, this study demonstrates the first direct observation of SPPs in $Ti_3C_2T_x$ MXenes within the visible portion of the electromagnetic spectrum, specifically up to 1.9 eV. Using nP-PEEM and FDTD simulations, we demonstrate that SPPs are supported on MXene flakes that are thicker than 30 nm, while thinner flakes do not exhibit such modes. The reported modes do not exhibit a resonance. Above 1.9 eV, waveguide-like modes dominate the electromagnetic response of $Ti_3C_2T_x$. The findings highlight the critical role of flake shape, losses, and dielectric environment in determining the plasmonic properties of MXenes, paving the way for their potential application in plasmon-enhanced technologies. While this study focuses on $Ti_3C_2T_x$ MXenes, the results lay the groundwork for future exploration of MXene plasmonics with nP-PEEM. The tunability of MXenes, in terms of their transition metals and surface terminations, suggests exciting opportunities for developing applications, including plasmon-enhanced catalysis. Achieving strong-field confinement and enhanced light-matter interaction in the visible region will require modifying the strength and energy of the interband transition, a challenge that the synthetic tunability of MXenes holds notable potential to address.

MATERIALS AND METHODS
Sample preparation
Ti_3AlC_2 $M_{n+1}AX_n$ (MAX) phase (98% purity) was purchased from American Elements. $Ti_3C_2T_x$ flakes were synthesized using the Minimally Intensive Layer Delamination (MILD) approach as detailed in (68). This method uses a LiF/HCl mixture to produce hydrogen fluoride (HF) in situ to etch the aluminum layers of the parent MAX phase Ti_3AlC_2. Subsequently, the generated MXene stacks are washed and delaminated with deionized H_2O, resulting in a solution of $Ti_3C_2T_x$ stacks with mixed surface terminations (T_x = F, O, and OH) in H_2O. The solution was further diluted with H_2O and drop casted in 15-µl drops onto silicon substrates with ~2-nm native oxide. The silicon wafers [n-doped Si(100), ρ = 1 to 10 ohms] were purchased from University Wafer. Then, the substrate was heated up to 150°C to evaporate the water. This process produces separated flakes with lateral sizes of several microns (see figs. S1 to S3). The samples were transferred to ultrahigh vacuum (UHV) and annealed to ~200°C to desorb residual contaminants before the PEEM measurements (69). Atomic force microscopy was conducted in the tapping mode on a Bruker MM8 to determine the thickness of the flakes (see figs. S1 to S3).

PEEM experiments
All PEEM experiments were performed under UHV (base pressure, 1×10^{-10} mbar) using a photoelectron microscope from Focus GmbH. The microscope has a spatial resolution less than 40 nm. 1P-PEEM was carried out with a 100-W broadband mercury arc lamp ($h\nu \leq 5.1$ eV) under grazing incidence (65° to the surface normal) as illustrated in Fig. 1B.

Initially unoccupied intermediate states, such as plasmon resonances, may be pumped and probed in nP-PEEM (with $n \geq 2$) so that they may contribute to the PEEM signal. Monochromatic nP-PEEM (n = 2 to 4) experiments were conducted mostly with the fundamental ($1.35 \leq 1h\nu \leq 1.9$ eV, 5- to 30-nJ pulse energy, 30- to 40-fs pulse duration) or the second harmonic $2.7 \leq 2h\nu \leq 3.8$ eV, 5- to 30-nJ pulse energy, 40- to 60-fs pulse duration) of a homebuilt optical parametric amplifier (OPA). The OPA was pumped by the second harmonic ($2h\nu$ = 2.4 eV) of a Coherent Monaco with a repetition rate of 4 MHz. nP-PEEM measurements with $2h\nu$ = 2.4 eV were carried out with the second harmonic of the Coherent Monaco laser (2- to 3-nJ pulse energy, 180-fs pulse duration). The laser spot sizes on the sample were ~300 to 1000 µm^2.

The linearly polarized laser beam was directed to the sample either at grazing incidence (65° to the surface normal) or at near-normal incidence (4° to the surface normal) via a rhodium mirror inside the microscope column (see Fig. 1B). In the latter configuration, the laser polarization is effectively in the plane of the sample surface. $\lambda/2$ wave plates were used to tune the in-plane laser polarization with respect to the edges of the MXene stacks.

*n*P-PEEM results from two MXene flakes (flake 1 and flake 2) are presented in Results. The work function of both flakes is ~4.8 eV (see fig. S6). Hence, *n*P-PEEM experiments with photon energies $h\nu < 4.8$ eV correspond to 2P-PEEM, $h\nu < 2.4$ eV to 3P-PEEM, and $h\nu < 1.6$ eV to 4P-PEEM.

Simulations of surface polaritons

Two simulation approaches were carried out to assign the measured surface polaritons. Both approaches consider a stack consisting of a MXene flake with thickness *d* on top of 2-nm native SiO_2 on top of 300-μm silicon(100). The dielectric functions of the SiO_2 and silicon were obtained from the SOPRA data bank (www.sspectra.com/sopra.html) and the *Handbook of Optical Constants of Solids*, respectively (*70*).

We conducted our simulations using the recently reported dielectric function of $Ti_3C_2T_x$ (*23*). Our first theoretical approach is based on the transfer matrix method (*71, 72*). It uses the Fresnel coefficients to calculate the wave vector– and energy-dependent reflection coefficients $r(k_x, E)$ of the entire sample stack. The poles of the reflection coefficient correspond to the sample's polaritonic modes. They can be approximately found by assuming pure real wave vectors k_x and plotting the intensity map of the imaginary part of $r(k_x, E)$. This approach has been successfully used before to model polaritons observed with scattering near-field optical microscopy (*44, 73, 74*). Details and derivations can be found in the Supplementary Materials of (*44*). Similarly, we find the exact dispersion relation by numerically solving for poles of the reflection coefficient at a constant energy. We explicitly solve only for bound modes (fields that evanescently decay away from the interface) by choosing the values of the complex square root $k_z = \sqrt{\varepsilon(\omega)\frac{\omega^2}{c^2} - k_x^2}$ such that $Im(k_x) > 0$. To find the propagation lengths of the observed mode at 1.7 eV, k_x was calculated by the above method as a function of thickness, yielding $L_{SPP} = [Im(k_x)]^{-1}$ as a measure of in-plane decay. Once k_x is determined by this numerical method, the electric fields and Poynting vectors can be plotted analytically as done in fig. S4.

In our second theoretical approach, we performed FDTD simulations with Lumerical by Ansys (*75*). FDTD is a fully vectorial simulation method that can calculate time evolutions of electromagnetic fields by solving Maxwell's equations. FDTD simulations were used to determine the spatial and temporal field distributions within our sample stack with nanometer and femtosecond resolution. *n*P-PEEM images were reproduced on the basis of the electric fields from the FDTD output because the PEEM signal can be expressed by $\int dt \left(E_x + E_y + E_z\right)^{2n}$ where *n* is the number of photons in the photoemission process (*49, 50, 76*). A field-time monitor was used to record the time evolution of fields to simulate *n*P-PEEM images in Figs. 2E and 4 (A and B). The spatial distributions of the E_z fields of Fig. 2 (F to H) were calculated with a frequency-domain field profile monitor. Further details and example of *n*P-PEEM image simulations with FDTD can be found in (*76*).

Supplementary Materials

This PDF file includes:
Supplementary Text
Figs. S1 to S8

REFERENCES AND NOTES

1. V. Kamysbayev, A. S. Filatov, H. Hu, X. Rui, F. Lagunas, D. Wang, R. F. Klie, D. V. Talapin, Covalent surface modifications and superconductivity of two-dimensional metal carbide MXenes. *Science* **369**, 979–983 (2020).

2. D. Wang, C. Zhou, A. S. Filatov, W. Cho, F. Lagunas, M. Wang, S. Vaikuntanathan, C. Liu, R. F. Klie, D. V. Talapin, Direct synthesis and chemical vapor deposition of 2D carbide and nitride MXenes. *Science* **379**, 1242–1247 (2023).

3. C. Zhou, D. Wang, F. Lagunas, B. Atterberry, M. Lei, H. Hu, Z. Zhou, A. S. Filatov, D. Jiang, A. J. Rossini, R. F. Klie, D. V. Talapin, Hybrid organic–inorganic two-dimensional metal carbide MXenes with amido- and imido-terminated surfaces. *Nat. Chem.* **15**, 1722–1729 (2023).

4. B. Anasori, M. R. Lukatskaya, Y. Gogotsi, 2D metal carbides and nitrides (MXenes) for energy storage. *Nat. Rev. Mater.* **2**, 16098 (2017).

5. J. Zhang, Y. Zhao, X. Guo, C. Chen, C.-L. Dong, R.-S. Liu, C.-P. Han, Y. Li, Y. Gogotsi, G. Wang, Single platinum atoms immobilized on an MXene as an efficient catalyst for the hydrogen evolution reaction. *Nat. Catal.* **1**, 985–992 (2018).

6. S. Bai, M. Yang, J. Jiang, X. He, J. Zou, Z. Xiong, G. Liao, S. Liu, Recent advances of MXenes as electrocatalysts for hydrogen evolution reaction. *NPJ 2D Mater. Appl.* **5**, 78 (2021).

7. A. D. Dillon, M. J. Ghidiu, A. L. Krick, J. Griggs, S. J. May, Y. Gogotsi, M. W. Barsoum, A. T. Fafarman, Highly conductive optical quality solution-processed films of 2D titanium carbide. *Adv. Funct. Mater.* **26**, 4162–4168 (2016).

8. A. Gellé, T. Jin, L. de la Garza, G. D. Price, L. V. Besteiro, A. Moores, Applications of plasmon-enhanced nanocatalysis to organic transformations. *Chem. Rev.* **120**, 986–1041 (2019).

9. X. Tang, X. Fan, L. Yao, G. Li, M. Li, X. Zhao, Q. Hao, T. Qiu, Electromagnetic mechanisms or chemical mechanisms? Role of interfacial charge transfer in the plasmonic metal/semiconductor heterojunction. *J. Phys. Chem. Lett.* **13**, 7816–7823 (2022).

10. K. A. Willets, R. P. V. Duyne, Localized surface plasmon resonance spectroscopy and sensing. *Annu. Rev. Phys. Chem.* **58**, 267–297 (2007).

11. Z. Zhang, Y. Fang, W. Wang, L. Chen, M. Sun, Propagating surface plasmon polaritons: Towards applications for remote-excitation surface catalytic reactions. *Adv. Sci.* **3**, 1500215 (2016).

12. T. Low, A. Chaves, J. D. Caldwell, A. Kumar, N. X. Fang, P. Avouris, T. F. Heinz, F. Guinea, L. Martin-Moreno, F. Koppens, Polaritons in layered two-dimensional materials. *Nat. Mater.* **16**, 182–194 (2017).

13. F. H. da Jorna, L. Xian, A. Rubio, S. G. Louie, Universal slow plasmons and giant field enhancement in atomically thin quasi-two-dimensional metals. *Nat. Commun.* **11**, 1013 (2020).

14. E. Hwang, S. Das Sarma, Dielectric function, screening, and plasmons in two-dimensional graphene. *Phys. Rev. B* **75**, 205418 (2007).

15. Y. Liu, R. F. Willis, K. Emtsev, T. Seyller, Plasmon dispersion and damping in electrically isolated two-dimensional charge sheets. *Phys. Rev. B* **78**, 201403 (2008).

16. F. J. García de Abajo, Graphene plasmonics: Challenges and opportunities. *ACS Photonics* **1**, 135–152 (2014).

17. A. Elbanna, H. Jiang, Q. Fu, J.-F. Zhu, Y. Liu, M. Zhao, D. Liu, S. Lai, X. W. Chua, J. Pan, Z. X. Shen, L. Wu, Z. Liu, C.-W. Qiu, J. Teng, 2D material infrared photonics and plasmonics. *ACS Nano* **17**, 4134–4179 (2023).

18. D. B. Velusamy, J. K. El-Demellawi, A. M. El-Zohry, A. Giugni, S. Lopatin, M. N. Hedhili, A. E. Mansour, E. D. Fabrizio, O. F. Mohammed, H. N. Alshareef, MXenes for plasmonic photodetection. *Adv. Mater.* **31**, e1807658 (2019).

19. K. Hantanasirisakul, Y. Gogotsi, Electronic and optical properties of 2D transition metal carbides and nitrides (MXenes). *Adv. Mater.* **30**, 1804779 (2018).

20. Y.-Z. Zhang, Y. Wang, Q. Jiang, J. K. El-Demellawi, H. Kim, H. N. Alshareef, MXene printing and patterned coating for device applications. *Adv. Mater.* **32**, 1908486 (2020).

21. Á. Morales-García, F. Calle-Vallejo, F. Illas, MXenes: New horizons in catalysis. *ACS Catal.* **10**, 13487–13503 (2020).

22. K. Chaudhuri, M. Alhabeb, Z. Wang, V. M. Shalaev, Y. Gogotsi, A. Boltasseva, Highly broadband absorber using plasmonic titanium carbide (MXene). *ACS Photonics* **5**, 1115–1122 (2018).

23. A. A. Shamsabadi, H. Fang, D. Zhang, A. Thakur, C. Y. Chen, A. Zhang, H. Wang, B. Anasori, M. Soroush, Y. Gogotsi, Z. Fakhraai, The evolution of MXenes conductivity and optical properties upon heating in air. *Small Methods.* **7**, e2300568 (2023).

24. J. K. El-Demellawi, S. Lopatin, J. Yin, O. F. Mohammed, H. N. Alshareef, Tunable multipolar surface plasmons in 2D $Ti_3C_2T_x$ MXene flakes. *ACS Nano* **12**, 8485–8493 (2018).

25. X. Guo, N. Li, C. Wu, X. Dai, R. Qi, T. Qiao, T. Su, D. Lei, N. Liu, J. Du, E. Wang, X. Yang, Q. Dai, Studying plasmon dispersion of MXene for enhanced electromagnetic absorption. *Adv. Mater.* **34**, e2201120 (2022).

26. S. A. Mikhailov, K. Ziegler, New electromagnetic mode in graphene. *Phys. Rev. Lett.* **99**, 016803 (2007).

27. H. Lashgari, M. Abolhassani, A. Boochani, S. Elahi, J. Khodadadi, Electronic and optical properties of 2D graphene-like compounds titanium carbides and nitrides: DFT calculations. *Solid State Commun.* **195**, 61–69 (2014).

28. B. Huber, S. Pres, E. Wittmann, L. Dietrich, J. Lüttig, D. Fersch, E. Krauss, D. Friedrich, J. Kern, V. Lisinetskii, M. Hensen, B. Hecht, R. Bratschitsch, R. E. Riedle, T. Brixner, Space-and time-resolved UV-to-NIR surface spectroscopy and 2D nanoscopy at 1 MHz repetition rate. *Rev. Sci. Instrum.* **90**, 113103 (2019).

29. L. I. Chelaru, M. von Horn-von Hoegen, F.-J. Meyer zu Heringdorf, Fringe fields in nonlinear photoemission microscopy. *Phys. Rev. B* **73**, 115416 (2006).

30. F.-J. Meyer zu Heringdorf, L. I. Chelaru, S. Möllenbeck, D. Thien, M. von Horn-Hoegen, Femtosecond photoemission microscopy. *Surf. Sci.* **601**, 4700–4705 (2007).

31. R. C. Word, J. Fitzgerald, R. Könenkamp, Direct imaging of optical diffraction in photoemission electron microscopy. *Appl. Phys. Lett.* **103**, 021118 (2013).

32. R. C. Word, J. P. Fitzgerald, R. Könenkamp, Direct coupling of photonic modes and surface plasmon polaritons observed in 2-photon PEEM. *Opt. Express* **21**, 30507–30520 (2013).

33. M. Dąbrowski, Y. Dai, H. Petek, Ultrafast photoemission electron microscopy: Imaging plasmons in space and time. *Chem. Rev.* **120**, 6247–6287 (2020).

34. P. P. Joshi, R. Li, J. L. Spellberg, L. Liang, S. B. King, Nanoimaging of the edge-dependent optical polarization anisotropy of black phosphorus. *Nano Lett.* **22**, 3180–3186 (2022).

35. J. L. Spellberg, L. Kodaimati, P. P. Joshi, N. Mirzajani, L. Liang, S. B. King, Electronic structure orientation as a map of in-plane antiferroelectricity in β′-In₂Se₃. *Sci. Adv.* **10**, eado2136 (2024).

36. A. Boehm, S. D. Gennaro, C. F. Doiron, T. E. Beechem, M. B. Sinclair, I. Brener, R. Sarma, T. Ohta, Near-field imaging of optical resonances in silicon metasurfaces using photoelectron microscopy. *APL Photonics* **9**, 066103 (2024).

37. T. J. Davis, D. Janoschka, P. Dreher, B. Frank, F.-J. Meyer zu Heringdorf, H. Giessen, Ultrafast vector imaging of plasmonic skyrmion dynamics with deep subwavelength resolution. *Science* **368**, eaba6415 (2020).

38. Y. Dai, Z. Zhou, A. Ghosh, R. S. K. Mong, A. Kubo, C.-B. Huang, H. Petek, Plasmonic topological quasiparticle on the nanometre and femtosecond scales. *Nature* **588**, 616–619 (2020).

39. M. Dąbrowski, Y. Dai, H. Petek, Ultrafast microscopy: Imaging light with photoelectrons on the nano–femto scale. *J. Phys. Chem. Lett.* **8**, 4446–4455 (2017).

40. S. Sayan, E. Garfunkel, S. Suzer, Soft x-ray photoemission studies of the HfO₂/SiO₂/Si system. *Appl. Phys. Lett.* **80**, 2135–2137 (2002).

41. R. Li, G. Wildenberg, K. Boergens, Y. Yang, K. Weber, J. Rieger, A. Arcidiacono, R. Klie, N. Kasthuri, S. B. King, OsO₄ as the contrast-generating chemical species of osmium-stained biological tissues in electron microscopy. *Chembiochem* **25**, e202400311 (2024).

42. R. C. Word, J. Fitzgerald, R. Könenkamp, Light propagation and interaction observed with electrons. *Ultramicroscopy* **160**, 84–89 (2016).

43. P. Kahl, S. Wall, C. Witt, C. Schneider, D. Bayer, A. Fischer, P. Melchior, M. Horn-von Hoegen, M. Aeschlimann, F.-J. Meyer zu Heringdorf, Normal-incidence photoemission electron microscopy (NI-PEEM) for imaging surface plasmon polaritons. *Plasmonics* **9**, 1401–1407 (2014).

44. S. Dai, Z. Fei, Q. Ma, A. S. Rodin, M. Wagner, A. S. McLeod, M. K. Liu, W. Gannett, W. Regan, K. Watanabe, T. Taniguchi, M. Thiemens, G. Dominguez, A. H. C. Neto, A. Zettl, F. Keilmann, P. Jarillo-Herrero, M. M. Fogler, D. N. Basov, Tunable phonon polaritons in atomically thin van der Waals crystals of boron nitride. *Science* **343**, 1125–1129 (2014).

45. C. Lemke, T. Leißner, A. Klick, J. Fiutowski, J. W. Radke, M. Thomaschewski, J. Kjelstrup-Hansen, H.-G. Rubahn, M. Bauer, The complex dispersion relation of surface plasmon polaritons at gold/para-hexaphenylene interfaces. *Appl. Phys. B* **116**, 585–591 (2014).

46. A. Miranda, J. Halim, M. Barsoum, A. Lorke, Electronic properties of freestanding Ti₃C₂Tₓ MXene monolayers. *Appl. Phys. Lett.* **108**, 033102 (2016).

47. K. Yamagiwa, M. Shibuta, A. Nakajima, Two-photon photoelectron emission microscopy for surface plasmon polaritons at the Au (111) surface decorated with alkanethiolate self-assembled monolayers. *Phys. Chem. Chem. Phys.* **19**, 13455–13461 (2017).

48. M. Benchakar, L. Loupias, C. Garnero, T. Bilyk, C. Morais, C. Canaff, N. Guignard, S. Morisset, H. Pazniak, S. Hurand, P. Chartier, J. Pacaud, V. Mauchamp, M. W. Barsoum, A. Habrioux, S. Célérier, One MAX phase, different MXenes: A guideline to understand the crucial role of etching conditions on Ti₃C₂Tₓ surface chemistry. *Appl. Surf. Sci.* **530**, 147209 (2020).

49. Y. Dai, M. Dąbrowski, V. A. Apkarian, H. Petek, Ultrafast microscopy of spin-momentum-locked surface plasmon polaritons. *ACS Nano* **12**, 6588–6596 (2018).

50. D. Podbiel, P. Kahl, A. Makris, B. Frank, S. Sindermann, T. J. Davis, H. Giessen, M. H. Hoegen, F.-J. Meyer zu Heringdorf, Imaging the nonlinear plasmoemission dynamics of electrons from strong plasmonic fields. *Nano Lett.* **17**, 6569–6574 (2017).

51. F. Crameri, G. E. Shephard, P. J. Heron, The misuse of colour in science communication. *Nat. Commun.* **11**, 5444 (2020).

52. F. Crameri, Scientific colour maps, Zenodo Version 8.0.1 (2021). 10.5281/zenodo.8409685.

53. H. Raether, *Surface Plasmons on Smooth and Rough Surfaces and on Gratings* (Springer, 1988).

54. H. Raether, *Excitation of Plasmons and Interband Transitions by Electrons* (Springer-Verlag, 1980).

55. P. Berini, Long-range surface plasmon polaritons. *Adv. Opt. Photonics* **1**, 484–588 (2009).

56. M. Dąbrowski, Y. Dai, A. Argondizzo, Q. Zou, X. Cui, H. Petek, Multiphoton photoemission microscopy of high-order plasmonic resonances at the Ag/Vacuum and Ag/Si interfaces of epitaxial silver nanowires. *ACS Photonics* **3**, 1704–1713 (2016).

57. B. Frank, P. Kahl, D. Podbiel, G. Spektor, M. Orenstein, L. Fu, T. Weiss, M. H. Hoegen, T. J. Davis, F.-J. Meyer zu Heringdorf, H. Giessen, Short-range surface plasmonics: Localized electron emission dynamics from a 60-nm spot on an atomically flat single-crystalline gold surface. *Sci. Adv.* **3**, e1700721 (2017).

58. M. Großmann, M. Black, J. Jaruschewski, A. Klick, T. Leißner, J. Fiutowski, H.-G. Rubahn, M. Bauer, Micro-spectroscopy of buried short-range surface plasmon polaritons supported by thin polycrystalline gold films. *Plasmonics* **16**, 737–746 (2021).

59. J. Burke, G. Stegeman, T. Tamir, Surface-polariton-like waves guided by thin, lossy metal films. *Phys. Rev. B.* **33**, 5186 (1986).

60. P. Berini, Plasmon-polariton waves guided by thin lossy metal films of finite width: Bound modes of asymmetric structures. *Phys. Rev. B.* **63**, 125417 (2001).

61. N. M. Buckanie, P. Kirschbaum, S. Sindermann, F.-J. Meyer zu Heringdorf, Interaction of light and surface plasmon polaritons in Ag Islands studied by nonlinear photoemission microscopy. *Ultramicroscopy* **130**, 49–53 (2013).

62. V. Mauchamp, M. Bugnet, E. P. Bellido, G. A. Botton, P. Moreau, D. Magne, M. Naguib, T. Cabioc'h, M. W. Barsoum, Enhanced and tunable surface plasmons in two-dimensional Ti₃C₂ stacks: Electronic structure versus boundary effects. *Phys. Rev. B.* **89**, 235428 (2014).

63. J. Nelayah, M. Kociak, O. Stéphan, N. Geuquet, L. Henrard, F. J. García de Abajo, I. Pastoriza-Santos, L. M. Liz-Marzán, C. Colliex, Two-dimensional quasistatic stationary short range surface plasmons in flat nanoprisms. *Nano Lett.* **10**, 902–907 (2010).

64. P. Berini, Plasmon-polariton waves guided by thin lossy metal films of finite width: Bound modes of symmetric structures. *Phys. Rev. B* **61**, 10484–10503 (2000).

65. H. Fang, Z. Fang, A. Thakur, B. Anasori, A. M. Rappe, Z. Fakhraai, Signatures of band-like optical and charge transport in Ti3C2Tx MXene flakes. ChemRxiv [Preprint] (2024). http://dx.doi.org/10.26434/chemrxiv-2024-rpf17.

66. T. Hu, H. Zhang, J. Wang, Z. Li, M. Hu, J. Tan, P. Hou, F. Li, X. Wang, Anisotropic electronic conduction in stacked two-dimensional titanium carbide. *Sci. Rep.* **5**, 16329 (2015).

67. J. Hadler-Jacobsen, F. H. Fagerli, H. Kaland, S. K. Schnell, Stacking sequence, interlayer bonding, termination group stability and Li/Na/Mg diffusion in MXenes. *ACS Mater. Lett.* **3**, 1369–1376 (2021).

68. M. Alhabeb, K. Maleski, B. Anasori, P. Lelyukh, L. Clark, S. Sin, Y. Gogotsi, Guidelines for synthesis and processing of two-dimensional titanium carbide (Ti₃C₂Tₓ MXene). *Chem. Mater.* **29**, 7633–7644 (2017).

69. T. Schultz, N. C. Frey, K. Hantanasirisakul, S. Park, S. J. May, V. B. Shenoy, Y. Gogotsi, N. Koch, Surface termination dependent work function and electronic properties of Ti₃C₂Tₓ MXene. *Chem. Mater.* **31**, 6590–6597 (2019).

70. A. Borghesi, G. Guizzetti, E. Palik, *Handbook of Optical Constants of Solids* (Elsevier, 1991).

71. N. C. Passler, A. Paarmann, Generalized 4 × 4 matrix formalism for light propagation in anisotropic stratified media: Study of surface phonon polaritons in polar dielectric heterostructures. *J. Opt. Soc. Am. B.* **34**, 2128–2139 (2017).

72. N. C. Passler, X. Ni, G. Carini, D. N. Chigrin, A. Alù, A. Paarmann, Layer-resolved resonance intensity of evanescent polariton modes in anisotropic multilayers. *Phys. Rev. B.* **107**, 235426 (2023).

73. Z. Zheng, J. Chen, Y. Wang, X. Wang, X. Chen, P. Liu, J. Xu, W. Xie, H. Chen, S. Deng, N. Xu, Highly confined and tunable hyperbolic phonon polaritons in van der Waals semiconducting transition metal oxides. *Adv. Mater.* **30**, 1705318 (2018).

74. F. Mooshammer, S. Chae, S. Zhang, Y. Shao, S. Qiu, A. Rajendran, A. J. Sternbach, D. J. Rizzo, X. Zhu, P. J. Schuck, J. C. Hone, D. N. Basov, In-plane anisotropy in biaxial ReS2 crystals probed by nano-optical imaging of waveguide modes. *ACS Photonics* **9**, 443–451 (2022).

75. A. Taflove, S. C. Hagness, M. Piket-May, "Computational electromagnetics: The finite-difference time-domain method" in *The Electrical Engineering Handbook* (Elsevier Inc., 2005), pp. 629–670.

76. A. Ghosh, S. Yang, Y. Dai, Z. Zhou, T. Wang, C.-B. Huang, H. Petek, A topological lattice of plasmonic merons. *Appl. Phys. Rev.* **8**, 041413 (2021).